Computers and Chemical Engineering 177 (2023) 108326

Contents lists available at ScienceDirect

Computers and Chemical Engineering

journal homepage: www.elsevier.com/locate/cace

Improved energy graph-based visualisation fault detection and isolation — A spectral theorem approach

Wikus Wolmarans [a,1], George van Schoor [b,1], Kenneth R. Uren [a,*,1]

[a] School of Electrical, Electronic and Computer Engineering, Faculty of Engineering, North-West University, Potchefstroom, 2531, South Africa
[b] Unit for Energy and Technology Systems, Faculty of Engineering, North-West University, Potchefstroom, 2531, South Africa

ARTICLE INFO

Keywords:
Energy graph-based visualisation
Fault detection
Fault isolation
Spectral theorem

ABSTRACT

This paper illustrates how the energy graph-based visualisation (EGBV) fault detection and isolation (FDI) method may be interpreted in terms of the spectral theorem to gain insight into the sensitivity and robustness performance of the method. It is shown that the EGBV monitoring structure can be decomposed into components of varying importance. A formula is proposed as a guideline for informed component removal. These principles are applied to a practical heated two-tank process. It is shown that lesser-weighted components exhibit noisy behaviour and, when removed, increase the robustness of EGBV. Additionally, the computational requirements for the EGBV method and its fault signatures are reduced. It is also shown that retaining smaller components provides the benefit of improved sensitivity. Therefore, a trade-off exists between sensitive and robust process monitoring. Furthermore, it is acknowledged that component removal may compromise the resolution of EGBV's fault signatures and so, a formula is derived to verify its resolution integrity.

1. Introduction

It is well known that industrial plants are becoming more complex and thus more prone to process faults. This increase in complexity may be attributed to multiple drivers, the most prominent of which are environmental regulations (Reis and Gins, 2017; van Schoor and Uren, 2018), increased safety requirements (Chen et al., 2017) and increased cost-effectiveness (Chen, 2011; Izadi et al., 2009). Additionally, overall performance increase (Chen, 2011), improved product quality (Chen et al., 2017) and production reliability (Qin, 2009) are all factors leading to plant owners expanding their facilities, hereby increasing its complexity. The standard alarm philosophies used by these plants have become increasingly ineffective as a result (Izadi et al., 2009) and therefore, the need exists for the development of more sophisticated fault monitoring schemes. Moreover, when considering the magnitude of societal and economic impact in the event of, for example, a refinery or power generation facility failure, the requirement of advanced monitoring schemes is easily justified.

The topic of advanced industrial fault monitoring is actively researched and several methods have been developed in response. A three-part, comprehensive review of dominant fault detection and isolation (FDI) techniques has been published by Venkatasubramanian et al. (2003a,b,c), which defines two main categories for FDI methods, namely *model-based* and *process history-based* (also referred to as data-driven (Gao et al., 2015)) approaches. Within the latter category, principal component analysis (PCA) is arguably the most well-known and applied FDI technique. Its application in practice (Russel et al., 2000; Nomikos and MacGregor, 1994) and its use in several comparison studies (Adil et al., 2016; Yin et al., 2012) have established PCA as a benchmark FDI method. However, these studies reveal that none of the FDI methods, including PCA, are without shortcomings, leading to the development of hybrid FDI approaches (Severson et al., 2016; Md Nor et al., 2020; Park et al., 2020).

A hybrid FDI approach can be understood as an amalgamation of existing FDI methods (Gao et al., 2015). It serves to improve upon the shortcomings of the original FDI methods. Examples include the work of Chiang et al. (2015) which combines modified distance and causal dependency methods for the diagnosis of unknown faults in the Tennessee Eastman process, as well as the work of Lee et al. (2003), which shows that the combination of Partial Least Squares (PLS) and a signed digraph (SDG) provides improved diagnosis of multiple faults. Escobar et al. (2017) combine generative topographic mapping and graph theory to extract relevant information for similarity assessment of distinct samples, while minimising the impact of unnecessary features. By combining these methodologies, improved discrimination and visualisation can be achieved.

* Corresponding author.
E-mail address: kenny.uren@nwu.ac.za (K.R. Uren).
[1] All authors contributed equally.

https://doi.org/10.1016/j.compchemeng.2023.108326
Received 14 December 2022; Received in revised form 18 April 2023; Accepted 5 June 2023
Available online 8 June 2023

Similarly, the *energy graph-based visualisation* (EGBV) FDI method combines model- and process history-based principles in the energy domain to gain a simplified but holistic view of the process for process monitoring (van Schoor and Uren, 2018). Fault monitoring within the energy and exergy domain has shown promising results (Marais et al., 2019; Greyling et al., 2022), particularly EGBV, which warrants further investigation for expansion and improvement.

In this work, it is shown that the EGBV method may be improved by the use of spectral decomposition, as it provides a theoretical basis for better understanding the method's FDI sensitivity and robustness performance such that either sensitivity or robustness may be prioritised. The validity of this improvement is shown in a practical process.

The paper is structured as follows: Section 2 describes the general theoretical foundation of EGBV as a precursor to the paper contribution in Section 4, which presents the theory of EGBV spectral decomposition. A practical case study is given in Section 5 and the results are discussed in Section 6. The paper is concluded in Section 7.

2. Energy graph-based visualisation

2.1. Introduction

Energy and exergy provide an ideal platform for the unified explanation of chemical, mechanical and electrical interactions within a process. In the work of Nikulshin et al. (2002), it is noted that exergetic analysis is rather useful for efficiency calculation, yet it is underutilised owing to the complexities of detailed thermodynamic modelling. He then shows how a graph approach is a suitable solution to provide a simple, holistic view of a process in terms of exergy transfers. Similarly, Van Schoor et al. (2014) more recently introduced the concept of energy as the unifying monitoring parameter for large-scale industrial processes, leading to further studies dedicated to the development of two main systematic approaches to achieving this, while simultaneously applying it to different processes. The first approach, namely *enthalpy–entropy monitoring* was applied by Du Rand and Van Schoor (2012a,b) on a generation IV high-temperature gas-cooled reactor (HTGR). Marais et al. (2016) extended this method to an auto thermal reformer process. The second approach, akin to Nikulshin et al. (2002), relies on an energy–exergy graph description of the process, followed by graph matching and finally eigendecomposition for fault monitoring. This method is referred to as *energy graph-based visualisation* (EGBV). The work of Uren et al. (2020) and Neser et al. (2021) demonstrate the application of EGBV on a trans-critical CO_2 heat pump and a Brayton cycle power conversion unit, respectively. Both approaches were shown to be effective. Since this work aims to extend the latter method, only a brief explanation of the EGBV method will be given. Detailed explanations may be found in Neser et al. (2021), Uren et al. (2020, 2018).

2.2. Theoretical principles

From van Schoor and Uren (2018) it follows that multi-domain processes can be explained simply through the use of attributed graphs. A graph in this context refers to a set of nodes and links, where the links describe a relationship between relevant nodes (Wilson, 1996). More specifically, an *attributed graph* allows for the inclusion of quantitative information of the structure analysed (Dehmer et al., 2017). When a process is described using an attributed graph, the nodes may represent process components and the links describe interactions between the components. Conveniently, energy may be used as the attribute for links since it applies to mechanical, chemical, electrical, and thermo-fluid interactions. Exergy, as a measure of energy quality (Çengel and Boles, 2004), is used as node attributes.

A graph $\mathcal{G}$ for a given process is formally defined as (Uren et al., 2018):

$$\mathcal{G} = (\mathcal{N}, \mathcal{L}, \mathcal{A}), \tag{1}$$

where $\mathcal{N}$ contains all nodes and $\mathcal{L}$ contains all links. The set of node attributes is given by $\mathcal{A}$. The process must be viewed in terms of its energy and exergy characteristics and for this reason, $\mathcal{A}$ contains the rate of change in exergy at node i ($\Delta\dot{B}_i$) and also the set of energy transfer rates between node numbers i and j ($\dot{E}_{ij}$) as given by the links. Assuming a total of n nodes in $\mathcal{G}$, $\mathcal{A}$ is characterised by a node signature matrix $\mathbf{N}_s \in \mathbb{R}^{n\times n+1}$, with subscript s denoting the term *signature*. $\mathbf{N}_s$ is given by:

$$\mathbf{N}_s = \left[\begin{array}{c|cccccc} \overbrace{\Delta\dot{B}_1}^{\text{Node attr.}} & \overbrace{\dot{E}_{11} & \dot{E}_{12} & \dots & \dot{E}_{1j} & \dots & \dot{E}_{1n}}^{\text{Link attr.}} \\ \Delta\dot{B}_2 & \dot{E}_{21} & & & & & \\ \vdots & \vdots & & \ddots & & & \\ \Delta\dot{B}_i & \dot{E}_{i1} & & & \dot{E}_{ij} & & \\ \vdots & \vdots & & & & \ddots & \\ \Delta\dot{B}_n & \dot{E}_{n1} & & & & & \dot{E}_{nn} \end{array}\right]. \tag{2}$$

If energy transfer does not occur between two given nodes, the entry is made zero. The relevant equations for energy and exergy calculations may be found in Çengel and Boles (2004). For online process monitoring, it is required to calculate (2) for every k time instant, that is, calculating $\mathbf{N}_{s,k}$. It is also required to calculate $\mathbf{N}_{s,ref}$ - a node signature matrix that contains the ideal, targeted energy and exergy attributes of the normal operating condition (NOC) of the process. A continuous comparison between $\mathbf{N}_{s,ref}$ and $\mathbf{N}_{s,k}$ would reveal undesired process deviations, or *faults*, requiring a formal matrix comparison procedure. Since the applicable matrices are graphs it is only natural to consider graph matching a means of meaningful comparison and as such, EGBV has adopted the method introduced in Wilson and Martinez (1997) and Jouili and Tabbone (2009) namely the heterogeneous euclidean overlap metric (HEOM). The comparison of $\mathbf{N}_{s,ref}$ and $\mathbf{N}_{s,k}$ with a number of attribute columns is therefore given by a cost matrix $\mathbf{C}_k \in \mathbb{R}^{n\times n}$ and its entries $c_{ij,k}$ are given by:

$$c_{ij,k} = \sqrt{\sum_{a=1}^{n+1}\left[\frac{|\mathbf{N}_{s,ref}(i,a) - \mathbf{N}_{m,k}(j,a)|}{\{range\}_a}\right]^2}, \tag{3}$$

with

$$\{range\}_a = |max_a - min_a|. \tag{4}$$

If the result of (4) is zero, then $\{range\}_a$ is set equal to one. Thus, the matrix $\mathbf{C}_k$ acts as a distance descriptor between $\mathbf{N}_{s,ref}$ and $\mathbf{N}_{s,k}$. Using (3) to compare $\mathbf{N}_{s,ref}$ with itself will result in $\mathbf{C}_{ref}$, which acts as the reference distance descriptor as it is based on NOC. Finally, eigendecomposition is applied to $\mathbf{C}_k$ (van Graan et al., 2017; Strang, 2009):

$$\mathbf{C}_k = \mathbf{Z}_k\mathbf{\Lambda}_k\mathbf{Z}_k^T, \tag{5}$$

where the columns of $\mathbf{Z}_k \in \mathbb{R}^{n\times n}$ are the eigenvectors $\mathbf{z}_1, \mathbf{z}_2, \dots, \mathbf{z}_i, \dots, \mathbf{z}_n$ corresponding to the eigenvalues λ_1, λ_2, …, λ_i, …, λ_n in the diagonal matrix $\mathbf{\Lambda}_k \in \mathbb{R}^{n\times n}$. Essentially, the purpose of (5) is to diagonalise $\mathbf{C}_k$ such that its structural information becomes known, revealing its hidden characteristics (van Schoor and Uren, 2018). The same procedure is followed for $\mathbf{C}_{ref}$. Now, each eigenvalue at time k may be normalised using its NOC counterpart:

$$\tilde{\lambda}_{i,k} = \left|\frac{\lambda_{i,k}}{\lambda_{i,ref}}\right| \tag{6}$$

Similarly, the normalised eigenvector entries of matrix $\mathbf{Z}_k$ are given by:

$$\tilde{z}_{ij,k} = \left|\frac{z_{ij,k}}{z_{ij,ref}}\right| \tag{7}$$

The complete set of $\tilde{\lambda}_{i,k}$ and $\tilde{z}_{ij,k}$ may be collectively referred to as eigenelements and are stacked into a monitoring matrix $\mathbf{\Phi}_k \in \mathbb{R}^{(n+1)\times n}$:

$$\mathbf{\Phi}_k = \begin{bmatrix} \tilde{\lambda}_{1,k} & \tilde{\lambda}_{2,k} & \cdots & \tilde{\lambda}_{i,k} & \cdots & \tilde{\lambda}_{n,k} \\ \hline \tilde{z}_{11,k} & \tilde{z}_{12,k} & \cdots & \tilde{z}_{1j,k} & \cdots & \tilde{z}_{1n,k} \\ \tilde{z}_{21,k} & & & & & \\ \vdots & & \ddots & & & \\ \tilde{z}_{i1,k} & & & \tilde{z}_{ij,k} & & \\ \vdots & & & & \ddots & \\ \tilde{z}_{n1,k} & & & & & \tilde{z}_{nn,k} \end{bmatrix} \tag{8}$$

In the event of a process fault, a structural shift is expected to occur in $\mathbf{C}_k$, leading to deviations occurring in the eigenelements in $\mathbf{\Phi}_k$. These deviations may be compared to thresholds to discern fault-driven deviations from normal process deviations. Let UTh_{ij} be the upper threshold of the eigenelement ϕ_{ij} in $\mathbf{\Phi}$ and let LTh_{ij} be the lower threshold of ϕ_{ij}, then a fault is declared if (Uren et al., 2020):

$$\phi_{ij,k} > UTh_{ij} \tag{9}$$

or if

$$\phi_{ij,k} < LTh_{ij}. \tag{10}$$

In EGBV, the fault detection thresholds are determined according to a desired false alarm rate (FAR). Thus, the values for UTh_{ij} and LTh_{ij} may be obtained empirically by first calculating $\mathbf{\Phi}_k$ from an NOC data set. Then, UTh_{ij} and LTh_{ij} are fitted to each eigenelement until the desired FAR for said eigenelement is achieved.

Therefore, if *any* $\phi_{ij,k}$ in $\mathbf{\Phi}_k$ violates its threshold, a fault is detected. This summarises the fault detection philosophy of EGBV. For fault isolation, a qualitative approach is taken where a symbol $\mathbb{f}_{ij,k}$ is assigned to the state of each $\phi_{ij,k}$ with reference to its thresholds. From Uren et al. (2020) and Neser et al. (2021), the following procedure is followed:

- If the condition of (9) holds true, then $\mathbb{f}_{ij,k}$ is assigned a '+1' symbol.
- If the condition of (10) holds true, then $\mathbb{f}_{ij,k}$ is assigned a '−1' symbol.
- If neither of these conditions is met, that is, when $LTh_{ij} \geq \phi_{ij,k} \geq UTh_{ij}$, then a '0' is assigned to $\mathbb{f}_{ij,k}$.

The symbols of all $\phi_{ij,k}$ may be captured in a symbolic matrix $\boldsymbol{\mathcal{F}}_k$ that is equal to $\mathbf{\Phi}_k$ in size:

$$\boldsymbol{\mathcal{F}}_k = \begin{bmatrix} \mathbb{f}_{11,k} & \mathbb{f}_{12,k} & \cdots & \mathbb{f}_{1j,k} & \cdots & \mathbb{f}_{1n,k} \\ \mathbb{f}_{21,k} & & & & & \\ \vdots & & \ddots & & & \\ \mathbb{f}_{i1,k} & & & \mathbb{f}_{ij,k} & & \\ \vdots & & & & \ddots & \\ \mathbb{f}_{(n+1),1,k} & & & & & \mathbb{f}_{(n+1),n,k} \end{bmatrix} \tag{11}$$

The $\boldsymbol{\mathcal{F}}$ matrix acts as the fault signature result. This enables fault isolation, as each fault produces a unique $\boldsymbol{\mathcal{F}}$. Additionally, the fault signature itself need not be determined on a sample-by-sample basis, that is, the calculation of a $\boldsymbol{\mathcal{F}}_k$ - a moving average approach ($\boldsymbol{\mathcal{F}}_{avg}$) may be more feasible for accurate classification in noisy processes (Uren et al., 2020; Neser et al., 2021). In the next section, it is explained how the spectral theory may be used to improve $\mathbf{\Phi}_k$ and $\boldsymbol{\mathcal{F}}_k$.

3. Structural description of EGBV

This section expands on the graph concepts of Section 2.2, and explains the definition of *structures* and *descriptors* within the scope of this study as an informal introduction to the formal theory introduced in Section 4.

In (1), the formal definition of a graph was given which includes a node set $\mathcal{N}$, a link set $\mathcal{L}$ and an attribute set $\mathcal{A}$. Consider Fig. 1 which shows a simple graph consisting of four nodes (numbered circles) to constitute $\mathcal{N}$ and four links (solid lines) to make up $\mathcal{L}$. Assume that the nodes and links have attributes similar to that shown in (2), thus $\mathbf{N}_s \in \mathcal{A}$. The *structure* of $\mathcal{G}$ can be thought of as the relationship of the nodes with each other and is visible from the placement of links. Since $\mathbf{N}_s$ not only captures the values of the attributes, but inherits the latter links' placement in matrix format, it can be argued that $\mathbf{N}_s$ is in fact a structural descriptor of $\mathcal{G}$. More specifically, this is defined as the *visible structure* of $\mathcal{G}$.

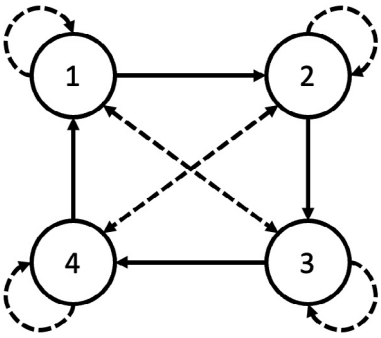

Fig. 1. Basic four-node graph showing the visible and invisible structure of the graph within the context of EGBV.

In Section 2.2, it is subsequently shown in (3) that when $\mathbf{N}_s$ matrices are compared to each other, the cost matrix $\mathbf{C}$ is obtained. One may think of $\mathbf{C}$ as a complete set of distances between the elements of $\mathbf{N}_s$. When these distances are illustrated as in Fig. 1 (shown as short-striped lines), it is apparent that they too contribute to the structural description of $\mathcal{G}$, except that they were hidden prior to the calculation of $\mathbf{C}$. Therefore $\mathbf{C}$, comprising these latent structure descriptors, are referred to as the *invisible structure* of $\mathcal{G}$.

Furthermore, within the invisible structure, two types of descriptors exist: *self-descriptors* and *cross-descriptors*. A self-descriptor is the distance from a node to itself, shown by the circular striped lines. The cross-descriptors are the diagonal striped lines showing the distance between different nodes. The former is captured on the main diagonal of $\mathbf{C}$, while the latter is given by the off-diagonal entries of $\mathbf{C}$. When considering $\mathbf{C}_{ref}$ specifically, one may refer to these self- and cross-descriptors as the *characteristic invisible structure*, because this is a special case where the self-descriptors are zero, and the cross-descriptors in the upper triangle of $\mathbf{C}$ is equal to its lower triangle counterpart, rendering $\mathbf{C}_{ref}$ symmetric. The latter property is exploited by the spectral theorem and is formally described in the next section.

4. Spectral analysis of EGBV

4.1. Introduction and applicability

The spectral theorem, when interpreted in its *sum of rank one projections* version, states that a given matrix $\mathbf{A} \in \mathbb{R}^{n\times n}$ may be rewritten as

$$\mathbf{A} = \lambda_1 \mathbf{u}_1 \mathbf{u}_1^T + \lambda_2 \mathbf{u}_2 \mathbf{u}_2^T + \cdots + \lambda_n \mathbf{u}_n \mathbf{u}_n^T, \tag{12}$$

with λ as the eigenvalues of $\mathbf{A}$ and $\mathbf{u}$ as the corresponding orthonormal eigenvectors, if $\mathbf{A} \in S_n$, where S_n denotes the set of real n dimensional symmetric matrices (Barrett, 2007). Eq. (12) makes it apparent that a different vantage point of analysis, so to speak, can be gained of the matrix being inspected as $\mathbf{A}$ has been decomposed into n independent terms (or components). A different vantage point in turn leads to potentially useful (and previously hidden) information being revealed.

While different fields of study benefit from the spectral theorem, a rather relevant example is PCA (Strang, 2009). In PCA, the eigendecomposition of the covariance matrix is equivalent to solving a line-of-best fit problem within a cluster of data points. In this case, the hidden information revealed is the values and directions of maximum variance within the data set (Pearson, 1901; Hotelling, 1933).

The spectral theorem is applicable to EGBV as well and more specifically, to $\mathbf{C}_{ref}$. This implies that $\mathbf{C}_{ref} \in \mathcal{S}_n \; \forall \; \mathbf{N}_{s,ref}$. While it is trivial to see that $\mathbf{C}_{ref} \in \mathbb{R}$ when using (3) since $\mathbf{N}_{s,ref} \in \mathbb{R}$, the symmetry property of $\mathbf{C}_{ref}$ needs to be proven formally.

Theorem 1. *The HEOM cost matrix* $\mathbf{C}_{ref} \in \mathcal{S}_n \; \forall \; \mathbf{N}_{s,ref}$.

Proof. Let c_{ij} be the (i,j)-th entry of $\mathbf{C}_{ref}$. First, (3) is rewritten as:

$$c_{ij} = \sqrt{\sum_{a=1}^{n+1} \frac{1}{\{range\}_a^2} |\mathbf{N}_{s,ref}(i,a) - \mathbf{N}_{s,ref}(j,a)|^2}. \tag{13}$$

Let $f(i,j,a)$ be given by:

$$f(i,j,a) = |\mathbf{N}_{s,ref}(i,a) - \mathbf{N}_{s,ref}(j,a)|^2, \tag{14}$$

such that

$$c_{ij} = \sqrt{\sum_{a=1}^{n+1} \frac{1}{\{range\}_a^2} f(i,j,a)}. \tag{15}$$

The expansion of $f(i,j,a)$ is given by:

$$f(i,j,a) = \mathbf{N}_{s,ref}^2(i,a) - 2\mathbf{N}_{s,ref}(i,a)\mathbf{N}_{s,ref}(j,a) + \mathbf{N}_{s,ref}^2(j,a). \tag{16}$$

Now, the (j,i)-th entry of $\mathbf{C}_{ref}$, c_{ji}, is given by:

$$c_{ij} = \sqrt{\sum_{a=1}^{n+1} \frac{1}{\{range\}_a^2} |\mathbf{N}_{s,ref}(j,a) - \mathbf{N}_{s,ref}(i,a)|^2}. \tag{17}$$

Therefore, its function $f(j,i,a)$ is given by:

$$f(j,i,a) = |\mathbf{N}_{s,ref}(j,a) - \mathbf{N}_{s,ref}(i,a)|^2, \tag{18}$$

which then expands to:

$$f(j,i,a) = \mathbf{N}_{s,ref}^2(j,a) - 2\mathbf{N}_{s,ref}(j,a)\mathbf{N}_{s,ref}(i,a) + \mathbf{N}_{s,ref}^2(i,a). \tag{19}$$

The terms in (19) may be rearranged to yield the following:

$$f(j,i,a) = \mathbf{N}_{s,ref}^2(i,a) - 2\mathbf{N}_{s,ref}(i,a)\mathbf{N}_{s,ref}(j,a) + \mathbf{N}_{s,ref}^2(j,a). \tag{20}$$

From (16) and (20), it is clear that $f(i,j,a) = f(j,i,a)$ and therefore that $c_{ij} = c_{ji}$. The latter equation implies that $\mathbf{C}_{ref} = \mathbf{C}_{ref}^T$ and by extension, that $\mathbf{C}_{ref}$ is symmetric. □

The $\mathbf{C}_{ref}$ matrix may therefore be re-written in the form

$$\mathbf{C}_{ref} = \lambda_1 \mathbf{z}_1 \mathbf{z}_1^T + \lambda_2 \mathbf{z}_2 \mathbf{z}_2^T + \cdots + \lambda_i \mathbf{z}_i \mathbf{z}_i^T + \cdots + \lambda_n \mathbf{z}_n \mathbf{z}_n^T, \tag{21}$$

with $\mathbf{z}_1, \mathbf{z}_2, \ldots, \mathbf{z}_i, \ldots, \mathbf{z}_n$ as the orthonormal eigenvectors in $\mathbf{Z}_{ref}$ corresponding to the eigenvalues $|\lambda_1| > |\lambda_2| > \ldots > |\lambda_i| > \ldots > |\lambda_n|$ in $\mathbf{\Lambda}_{ref}$. From their orthonormality, it is known that the euclidean norm for any $\mathbf{z}$ is given by $\|\mathbf{z}\|_2 = 1$ and by extension that $\|\mathbf{z}\mathbf{z}^T\|_2 = 1$. This implies that the eigenvalues act as weights for the terms in (21). The first term will have the most influence in describing $\mathbf{C}_{ref}$, while the last term will have the least. In summary, the spectral theorem allows for the decomposition of the characteristic invisible structure ($\mathbf{C}_{ref}$) of a process graph, given its real, symmetric properties in the form of a summation of separate components (or weighted terms), and the importance of each term is determined by the magnitude of the eigenvalue.

The significance of the weighted term view becomes clear when considering the presence of process noise during online monitoring. In Section 3, it is shown in (5) and (6) that the eigendecomposition is calculated for every kth process observation and normalised with $\mathbf{Z}_{ref}$ and $\mathbf{\Lambda}_{ref}$. It is expected that process noise introduced by $\mathbf{Z}_k$ and $\mathbf{\Lambda}_k$ will dominate the monitoring results of the $\tilde{z}_{ij,k}$ and $\tilde{\lambda}_{i,k}$ in $\mathbf{\Phi}_k$ that was normalised by $\lambda_{i,ref}$ and $z_{i,ref}$ that are among the lesser weighted terms of (21).

It would therefore be sensible to consider only the l most significant terms from (21) for $\mathbf{\Phi}_k$ and ignore the last $n - l$ terms to avoid noise contamination, while simultaneously reducing the number of eigenelements that need to be monitored. This is done by defining the reduced reference eigenvalue matrix $\mathbf{\Lambda}_{trim} \in \mathbb{R}^{l \times l}$:

$$\mathbf{\Lambda}_{trim} = \begin{bmatrix} \lambda_{1,ref} & 0 & \cdots & 0 \\ 0 & \lambda_{2,ref} & & \\ \vdots & & \ddots & \\ 0 & & & \lambda_{l,ref} \end{bmatrix}. \tag{22}$$

Subsequently, the reduced reference eigenvector matrix $\mathbf{Z}_{trim} \in \mathbb{R}^{n \times l}$ corresponding to $\mathbf{\Lambda}_{trim}$ is defined:

$$\mathbf{Z}_{trim} = \begin{bmatrix} \mathbf{z}_{1,ref} & \mathbf{z}_{2,ref} & \cdots & \mathbf{z}_{l,ref} \end{bmatrix}. \tag{23}$$

The definitions in (22) and (23) are equivalent to the PCA loading matrix $\mathbf{P}$ and define the *score space* for EGBV. The reduced monitoring matrix $\mathbf{\Phi}_{trim,k} \in \mathbb{R}^{(n+1) \times l}$ is then given by:

$$\mathbf{\Phi}_{trim,k} = \begin{bmatrix} \tilde{\lambda}_{1,k} & \tilde{\lambda}_{2,k} & \cdots & \tilde{\lambda}_{l,k} \\ \hline \tilde{z}_{11,k} & \tilde{z}_{12,k} & \cdots & \tilde{z}_{1l,k} \\ \tilde{z}_{21,k} & & & \\ \vdots & & \ddots & \\ \tilde{z}_{n1,k} & & & \tilde{z}_{nl,k} \end{bmatrix}. \tag{24}$$

Finally, since the symbolic fault signature matrix $\mathcal{F}_k$ is derived from $\mathbf{\Phi}_k$, it too reduces to $\mathcal{F}_{trim,k}$.

4.2. Selecting the number of components

The selection of l will significantly impact the FDI performance of EGBV. A too-large l will introduce process noise contamination and a too-small l may lead to missed detections due to an incomplete structural description of $\mathbf{C}$. An approach similar to that of the percent variance test (Russel et al., 2000) of PCA is proposed, with the key difference being that the eigenvalues do not represent variance coverage percentage as it does in PCA, but rather the total percentage of structural information retained of $\mathbf{C}_{ref}$. As such, it will be referred to here as the *percent structure* (PS) test. From (21) it is known that the eigenvalues act as weights in this structural description and so the PS for a given l may be determined the same way as PCA's percent variance:

$$PS(l) = \frac{\sum_{i=1}^{l} \mathbf{\Lambda}_{ref}(i,i)}{trace(\mathbf{\Lambda}_{ref})}. \tag{25}$$

It is acknowledged that the approach in (25) is rather subjective — the practitioner cannot be certain that the achieved PS is optimal for noise elimination in $\mathbf{C}_{ref}$. Even so, it remains a viable approach if a target PS is desired.

4.3. Verification of $\mathcal{F}_{trim}$ resolution

With the removal of lesser weighted components and the subsequent reduction of fault signatures, the resulting trim-med fault signatures $\mathcal{F}_{trim}$ will have less resolution when compared to the original signatures $\mathcal{F}$. The term *resolution* in the context of this work refers to the total number of unique faults that may be described by the fault signature. To this extent, a formula is derived for determining the resolution of $\mathcal{F}_{trim}$ such that its resolution may be verified.

A fault signature $\mathcal{F}$ will have the same size as the monitoring matrix $\mathbf{\Phi}$. When stated in terms of the number of graph nodes n, the size of $\mathcal{F}$ is $(n+1) \times n$. Recall from Section 2.2 that $\mathcal{F}$ is a qualitative matrix, where each entry has a set amount of symbols x. The philosophy explained in Section 2.2 assumes $x = 3$, but may also be chosen to be more or less, depending on the desired resolution. Therefore, the fault signature resolution R_f of a plant with n nodes and x symbol types is given by:

$$R_f = x^{n(n+1)} - 1. \tag{26}$$

The '−1' term removes the all-zero (fault-free) combination, such that R_f truly represents the theoretical number of faults that can be uniquely described. Now, the retained components l may be taken into account to determine the trimmed fault signature resolution $R_{f,trim}$:

$$R_{f,trim} = x^{l(n+1)} - 1. \tag{27}$$

The exponential nature of the formula reveals that a large $R_{f,trim}$ is easily achievable for large processes (having a large n), or a large x if the process is small. However, a small process with a low l will have limited resolution. The latter equation is useful to verify and avoid this scenario.

The main benefit of applying the spectral theorem to EGBV, is that it provides a theoretical basis for removing eigencomponents responsible for process noise, whereas the original EGBV method simply retained all eigencomponents. Furthermore, by only focusing on a subset of the eigencomponents, the real-time computational load of process monitoring as well as the storage requirements for fault signatures are significantly reduced. These benefits will become more prominent with process size. The theory of this section will now be demonstrated in a practical case study in the next section.

5. Case study

5.1. Process description

Fig. 2 shows a high-level process and instrumentation diagram (P&ID) of the process adapted from Uren et al. (2018). The steady-state values for the measured process variables (PVs) are summarised in Table 1. Its goal is to maintain pre-set liquid water levels L_1 in tank 1 and L_2 in tank 2, while also maintaining the temperature T_1 of the liquid in tank 1 and T_2 in tank 2. Both tank 1 and tank 2 contain agitators to improve heat transfer within the tank.

A cold water feed F_1 is fed to tank 1 from a cold water reservoir and at reservoir temperature $T_{1,in}$. The feed is controlled via valve 1 by a level controller LC1 based on L_1. The liquid is gravity-fed from tank 1 to tank 2. A hot water feed F_3 is fed at a pre-set temperature T_3 through coiled tubing into tank 1 for the purpose of heat transfer to the liquid content of tank 1 and exits tank 1 to a geyser for re-heating. The temperature of tank 1 is therefore controlled through TC1 by adjusting the hot water flow with valve 3.

Similar to tank 1, a cold water feed F_2 is fed to tank 2 from the same cold water reservoir used by tank 1 and at reservoir temperature $T_{2,in}$. Valve 2 is used to throttle F_2 based on the level L_2 observed by the level controller LC2. Additionally, a liquid feed is received from tank 1. The liquid is gravity-fed back to the cold water reservoir from tank 2. Hot water is circulated (at temperature T_4) through a coil into and out of tank 2 for heat transfer to the liquid in tank 2. T_2 is controlled by a temperature controller TC2 by throttling the hot water flow F_4 through the coil.

Given that each tank is required to maintain its level, the value for $F_{1,out}$, may be derived by the mass balance equation $F_{1,out} = F_1$. For tank 2, it holds that $F_{2,out} = F_{1,out} + F_2$.

Fig. 3 shows the physical pilot plant of the process and its descriptors are provided in Table 2. Tank 1 is situated highest on the structure, while tank 2 is placed lower enabling gravity feed from tanks 1 to 2.

The red motor housings on top of each tank show the agitators used to improve heat transfer within each tank. The blue tank below tank 2 is the cold water reservoir and the silver, cylindrical container to the right of tank 2 is the hot water reservoir. Item seven indicates the cold water heat exchange system, which acts outside the scope of the process to maintain the temperature of the cold water reservoir ($T_{1,in}$ and $T_{2,in}$). Likewise, the grey box indicated by item five serves the same purpose for the hot water reservoir (T_3 and T_4). Finally, the entire process is controlled autonomously by a Siemens S7-1200 programmable logic controller (PLC) unit housed in the orange control panel.

Table 1
Summary of average steady-state PV values.

Parameter	Value	Units
F_1	3.55×10^{-4}	[m^3/s]
F_2	1.68×10^{-4}	[m^3/s]
F_3	2.37×10^{-4}	[m^3/s]
F_4	2.37×10^{-4}	[m^3/s]
L_1	0.505	[m]
L_2	0.505	[m]
T_1	28	[°C]
$T_{1,in}$	25.2	[°C]
T_2	29	[°C]
$T_{2,in}$	25.6	[°C]
T_3	33	[°C]
T_4	33	[°C]

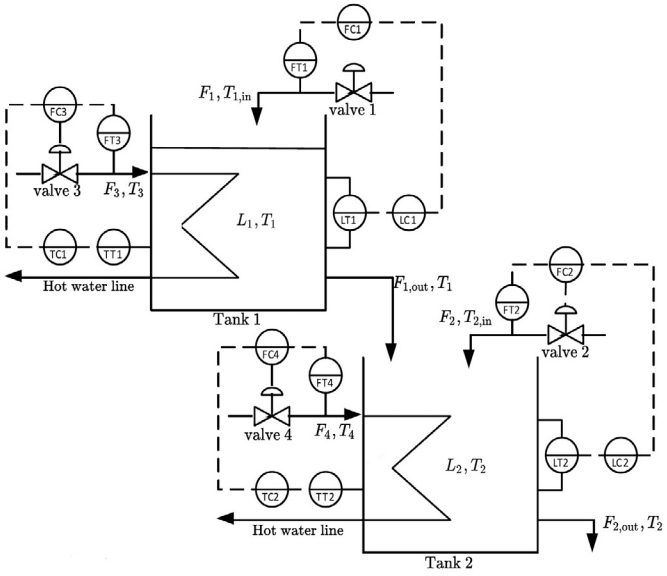

Fig. 2. P&ID of heated two-tank process.
Source: Adapted from Uren et al. (2018).

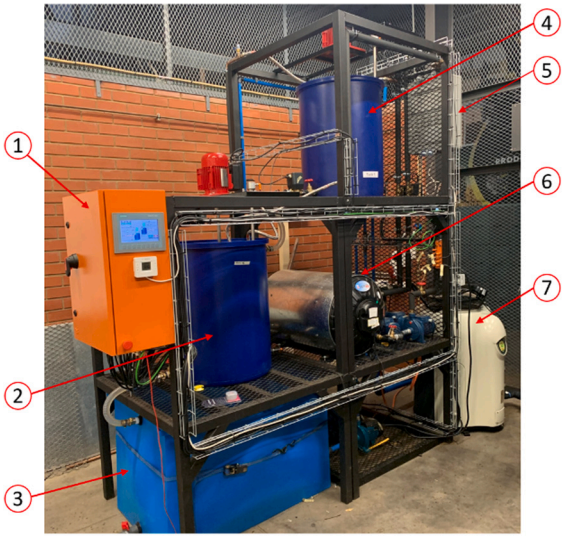

Fig. 3. Constructed pilot plant of the process in Fig. 2.

Table 2
Summary of components in Fig. 3.

Item	Description
1	Process local control panel
2	Tank 2
3	Cold water reservoir
4	Tank 1
5	Hot water heat exchange system
6	Hot water reservoir/geyser
7	Cold water heat exchange system

5.2. Application of EGBV

The application of EGBV in this particular process is already explained in Uren et al. (2018). As such, this section serves as contextual preamble to the section that follows, hence its inclusion in this work.

First, the attributed graph $\mathcal{G}$ must be developed in compliance with (1). This was done in Uren et al. (2018) and shown in Fig. 4(b). The heating coils within the tanks and the tanks themselves make up the node set $\mathcal{N}$. The mass flows and energy transfers within the process make up the link set $\mathcal{L}$. The attribute set $\mathcal{A}$ contains the energy transfer rates, as well as the rate of change in exergy of the links and nodes respectively to form the node signature matrix in (2) and is given by Uren et al. (2018):

$$\mathbf{N}_s = \left[\begin{array}{c|ccccc} \Delta\dot{B}_1 & \dot{E}_{11} & \dot{E}_{12} & \dot{E}_{13} & \dot{E}_{14} & \dot{E}_{15} \\ \Delta\dot{B}_2 & \dot{E}_{21} & \dot{E}_{22} & \dot{E}_{23} & \dot{E}_{24} & \dot{E}_{25} \\ \Delta\dot{B}_3 & \dot{E}_{31} & \dot{E}_{32} & \dot{E}_{33} & \dot{E}_{34} & \dot{E}_{35} \\ \Delta\dot{B}_4 & \dot{E}_{41} & \dot{E}_{42} & \dot{E}_{43} & \dot{E}_{44} & \dot{E}_{45} \\ \Delta\dot{B}_5 & \dot{E}_{51} & \dot{E}_{52} & \dot{E}_{53} & \dot{E}_{54} & \dot{E}_{55} \end{array}\right]. \tag{28}$$

As explained in Uren et al. (2018), the entries in $\mathbf{N}_s$ that do not represent in a link in Fig. 4(b) are made zero. Entries that show reverse direction notation of the same link are signed as negative. Finally, the rate of change in exergy of the environment external to the process ($\Delta\dot{B}_5$) is made zero. Thus, (28) reduces to:

$$\mathbf{N}_s = \left[\begin{array}{c|ccccc} \Delta\dot{B}_1 & 0 & \dot{E}_{12} & 0 & 0 & \dot{E}_{15} \\ \Delta\dot{B}_2 & -\dot{E}_{12} & 0 & \dot{E}_{23} & 0 & \dot{E}_{52} \\ \Delta\dot{B}_3 & 0 & -\dot{E}_{23} & 0 & -\dot{E}_{43} & \dot{E}_{35} \\ \Delta\dot{B}_4 & 0 & 0 & \dot{E}_{43} & 0 & \dot{E}_{45} \\ 0 & \dot{E}_{51} & \dot{E}_{52} & \dot{E}_{53} & \dot{E}_{54} & 0 \end{array}\right]. \tag{29}$$

For the energy transfer rate $\dot{E}$ of a fluid stream between node i and node j, the general formula (Çengel and Boles, 2004; Uren et al., 2018):

$$\dot{E}_{ij} = \dot{m}_{ij} c_p (T_{ij} - T_{ref}) \tag{30}$$

is used, with $\dot{m}_{ij}$ the mass flow rate for the fluid and c_p its specific heat capacity. The temperatures T_{ij} and T_{ref} represent the temperature of the stream and chosen reference temperature, respectively, with T_{ref} chosen as 0 °C. The same equation is applicable to links representing fluid-to-fluid heat transfer. If stream p is receiving heat energy from node i at node j, then (Çengel and Boles, 2004)

$$\dot{E}_{ij} = \dot{m}_p c_p (T_{p,out} - T_{p,in}). \tag{31}$$

There are no chemical reactions in this process and therefore only physical exergy transfer rate is applicable, given by:

$$\dot{B}_{ij} = \dot{m}\left[(h - h_0) - T_0(s - s_0)\right] \tag{32}$$

for fluid streams. For heat transfer, the following is used:

$$\dot{B}_{ij} = \left[1 - \frac{T_0}{T}\right]\dot{E}_{ij}. \tag{33}$$

Its specific enthalpy is denoted by h and the entropy by s. For any given node, the rate of change in exergy is calculated by:

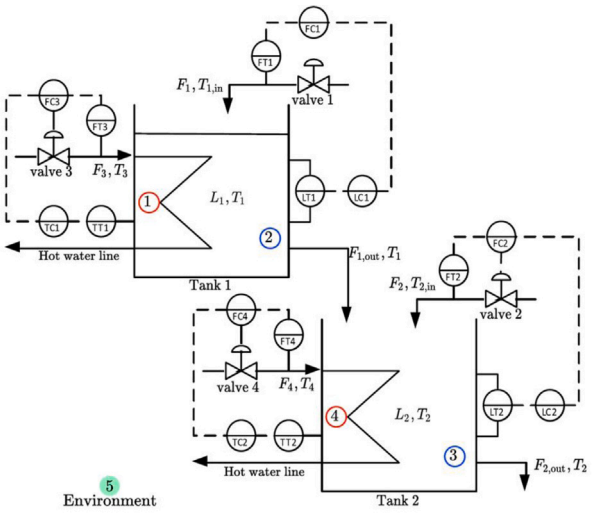

(a) P&ID with labelled nodes.

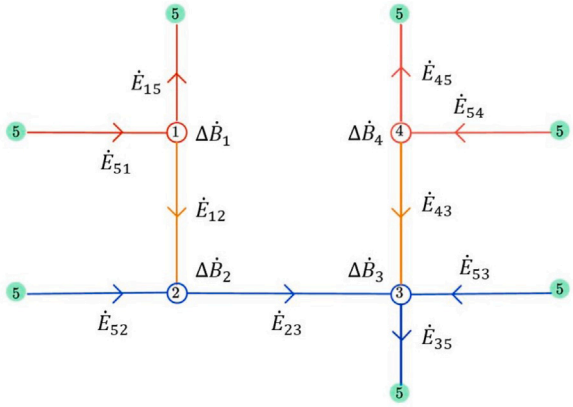

(b) Attributed graph $\mathcal{G}$ adapted from [30].

Fig. 4. Heated two-tank process.
Source: Adapted from Uren et al. (2018).

$$\Delta\dot{B} = \left(\sum \dot{B}_{ij}\right)_{in} - \left(\sum \dot{B}_{ij}\right)_{out}, \tag{34}$$

assuming steady-state operating conditions. Using (30) to (34) and Table 1, $\mathbf{N}_{s,ref}$ (in kW) is calculated as:

$$\mathbf{N}_{s,ref} = \left[\begin{array}{c|ccccc} 0.35 & 0 & 4.16 & 0 & 0 & 29.08 \\ -0.29 & -4.16 & 0 & 41.46 & 0 & -37.29 \\ -0.29 & 0 & -41.46 & 0 & -3.79 & 63.10 \\ 0.33 & 0 & 0 & 3.79 & 0 & 28.06 \\ 0 & 33.25 & 37.29 & 17.83 & 31.86 & 0 \end{array}\right]. \tag{35}$$

From this result, $\mathbf{C}_{ref}$ from (3) is determined to be:

$$\mathbf{C}_{ref} = \begin{bmatrix} 0 & 1.56 & 1.20 & 0.10 & 1.52 \\ 1.56 & 0 & 1.51 & 1.48 & 1.64 \\ 1.20 & 1.51 & 0 & 1.16 & 1.89 \\ 0.10 & 1.48 & 1.16 & 0 & 1.50 \\ 1.52 & 1.64 & 1.89 & 1.50 & 0 \end{bmatrix}. \tag{36}$$

The symmetry of $\mathbf{C}_{ref}$ is clear in (36) as a result of comparing $\mathbf{N}_{s,ref}$ with itself. Decomposing (36) into its eigenvalues and eigenvectors and sorting the eigenvalues according to magnitude yields

$$\mathbf{\Lambda}_{ref} = \begin{bmatrix} 5.56 & 0 & 0 & 0 & 0 \\ 0 & -2.29 & 0 & 0 & 0 \\ 0 & 0 & -1.82 & 0 & 0 \\ 0 & 0 & 0 & -1.34 & 0 \\ 0 & 0 & 0 & 0 & -0.11 \end{bmatrix}, \tag{37}$$

and

$$\mathbf{Z}_{ref} = \begin{bmatrix} -0.385 & -0.517 & 0.226 & -0.221 & 0.695 \\ -0.485 & 0.428 & -0.476 & -0.594 & 0.016 \\ -0.467 & -0.179 & -0.534 & 0.680 & -0.002 \\ -0.373 & -0.500 & 0.198 & -0.235 & -0.718 \\ -0.508 & 0.516 & 0.629 & 0.281 & -0.013 \end{bmatrix}, \tag{38}$$

which form the reference to which live monitored results $\mathbf{\Lambda}_k$ and $\mathbf{Z}_k$ are evaluated in the form of the monitoring matrix $\mathbf{\Phi}_k$ given in (11).

To calculate the thresholds UTh_{ij} and LTh_{ij} for $\mathbf{\Phi}_k$, a data set containing 900 observations of verified NOC data is used to first calculate $\mathbf{\Phi}_k$ for continuous, fault-free operation. Then, for each ϕ_{ij}, its UTh_{ij} is iteratively fitted to achieve a total false alarm rate (FAR) of 2.5%. The same is done for LTh_{ij}, such that each ϕ_{ij} achieves a FAR of 5%.

For an example of the fault detection results of EGBV, consider Fig. 5. The figure shows thirty graphs, each showing the trend of the entries ϕ_{ij} of $\mathbf{\Phi}$ over 1800 samples. The top row of the figure shows the normalised eigenvalues, as designated in (11). The column below every eigenvalue plot represents the entries of the corresponding normalised eigenvector. The upper and lower short-striped lines are the UTh and LTh of each ϕ_{ij}, respectively. For the first 900 samples, the process is operating at normal, steady-state conditions. It can be seen that during this period, all ϕ_{ij} remain mostly within their threshold, with occasional false alarm events. At sample 900, a 2% temperature sensor drift fault occurs and persists up to sample 1800. Now, it is shown how a subset of ϕ_{ij} violates either its UTh or LTh during this period, indicating that a process fault occurred, while other graphs show no clear change. Ideally, all ϕ_{ij} should respond to a fault, but since it has been defined in Section 5.2 that only a single threshold violation is required for fault detection, a fault state may be declared. Furthermore, a fault signature $\mathcal{F}$ may be compiled from these results. If the mean of each ϕ_{ij} for the entire fault period is evaluated against its thresholds for symbol assignment, then the fault signature is given by:

$$\mathcal{F}_{sensor} = \begin{bmatrix} 0 & -1 & 0 & 0 & 0 \\ 0 & 0 & 0 & 0 & -1 \\ -1 & 1 & 0 & 0 & 1 \\ -1 & 0 & 1 & -1 & 1 \\ 0 & 0 & 0 & 0 & 1 \\ 1 & -1 & 0 & 1 & 0 \end{bmatrix}, \tag{39}$$

acting as the unique identifier for the fault.

5.3. Components extraction

$\mathbf{C}_{ref}$ is rewritten in its rank one form according to the spectral theorem using the result in (37):

$$\begin{aligned} \mathbf{C}_{ref} = {} & 5.56\,(\mathbf{z}_1\mathbf{z}_1^T) - 2.29\,(\mathbf{z}_2\mathbf{z}_2^T) - 1.82\,(\mathbf{z}_3\mathbf{z}_3^T) \\ & - 1.34\,(\mathbf{z}_4\mathbf{z}_4^T) - 0.11\,(\mathbf{z}_5\mathbf{z}_5^T), \end{aligned} \tag{40}$$

which shows that eigenvalue λ_5 and its vector $\mathbf{z}_5$ have the least amount of contribution to the characteristic invisible structure and given its small magnitude relative to the other terms, is the most likely to introduce noise contamination in real-time monitoring results. A quick inspection of Fig. 5 would reveal that the right most ϕ_{ij} elements exhibit the most frequent false alarm triggers during samples 1 to 900. It would then be sensible to select $l = 4$ to define the score space. Using (25), it is determined that $PS(4) = 99.1\%$, meaning only 0.9% of the structural description of $\mathbf{C}_{ref}$ is lost.

5.4. Resolution verification

The formula given in (27) is used to verify the resolution of $\mathcal{F}_{trim}$ for this process. The philosophy of Section 2.2 is followed with $x = 3$. Then $R_{f,trim}$ is calculated:

$$R_{f,trim} = 3^{4(5+1)} - 1 = 2.82 \times 10^{11}, \tag{41}$$

which confirms that fault resolution is not a concern. Next, the selection of l is evaluated by considering the robustness and sensitivity of each eigenvalue and vector.

5.5. Robustness analysis

Robustness is generally defined as the resistance of a monitoring scheme to false alarms (Russel et al., 2000). Thus, having a low false alarm rate (FAR) is ideal. To this extent, the FAR results of each normalised eigenvalue $\tilde{\lambda}_i$ for five separate data sets that contain 900 observations of NOC state are calculated. These are independent of the data set on which the thresholds were calibrated. The results are shown in Fig. 6(a). Similarly, the FAR_{avg} of each normalised eigenvector $\tilde{\mathbf{z}}_i$, that is, the average FAR of all the vector entries, is calculated as a holistic performance metric for any given eigenvector. This is shown in Fig. 6(b). Note that due to the separate evaluation of FAR and FAR_{avg}, specific reference to $\tilde{\lambda}_i$ and $\tilde{\mathbf{z}}_i$ will be made, instead of the generic eigenelements designation ϕ_{ij}.

In Fig. 6(a), it is clear that $\tilde{\lambda}_1$ to $\tilde{\lambda}_4$ were able to repeat the FAR rate to which they were calibrated, within reasonable margin. This is in contrast to the FAR performance of $\tilde{\lambda}_5$, which distinctly shows the highest FAR rate for every data set. Evaluating the FAR_{avg} performance in Fig. 6(b) reveals the same trend. For all data sets, $\tilde{\mathbf{z}}_1$ to $\tilde{\mathbf{z}}_4$ produce results that are approximate to the 5% FAR to which they were calibrated, while $\tilde{\mathbf{z}}_5$ shows significantly higher FAR_{avg} rates for data sets three to five.

5.6. Sensitivity analysis

The sensitivity performance of the eigenvalues and eigenvectors is now evaluated, by studying the true alarm rates (TAR) of the normalised eigenvalues and vectors. Recall from Section 2 that the use of the residual space often exhibits superior sensitivity when compared to the score space. Fig. 5 is referred to once more, which shows that $\tilde{\lambda}_5$ and $\tilde{\mathbf{z}}_5$ have the most prominent response during fault state, suggesting superior sensitivity. To validate this observation, the true alarm rate (TAR) was calculated for twelve process faults detailed, which vary in type, magnitude and location. The TAR metric is used instead of the more popular missed detection rate (MDR) to ease the visual identification of outliers in the figures that follow.

Fig. 7(a) shows the TAR of all $\tilde{\lambda}_i$ during the process faults listed in Table 3. At first glance, a clear trend of sensitivity is not visible. For fault three, for example, $\tilde{\lambda}_1$ and $\tilde{\lambda}_2$ showed the best sensitivity. For fault eleven, $\tilde{\lambda}_2$ showed the best TAR. Regardless, $\tilde{\lambda}_5$ achieved the highest TAR percentage in nine of the twelve faults. Fig. 7(b) illustrates the TAR_{avg} performance of all $\tilde{\mathbf{z}}_i$. Once more, $\tilde{\lambda}_5$ shows the best sensitivity for nine of the twelve tested faults. The description of these process faults may be found in

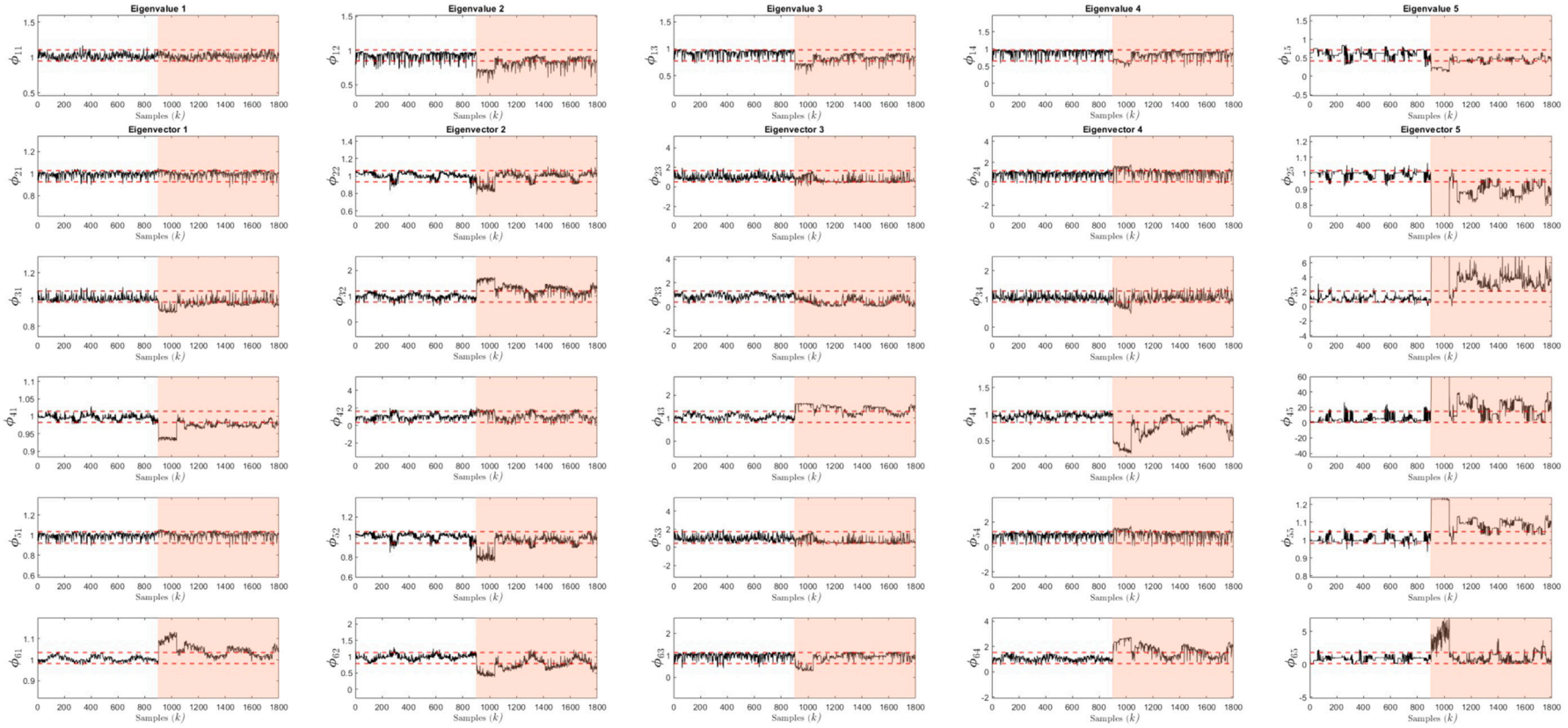

Fig. 5. Monitoring results of Φ over 1800 samples showing the detection of a 2% sensor drift in tank 2 at sample 900.

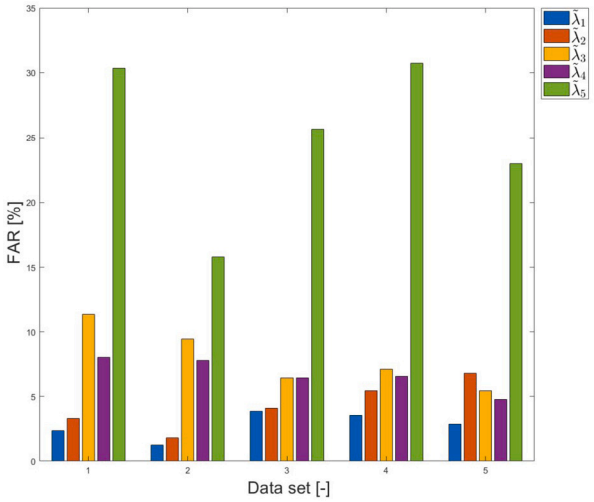

(a) FAR rates

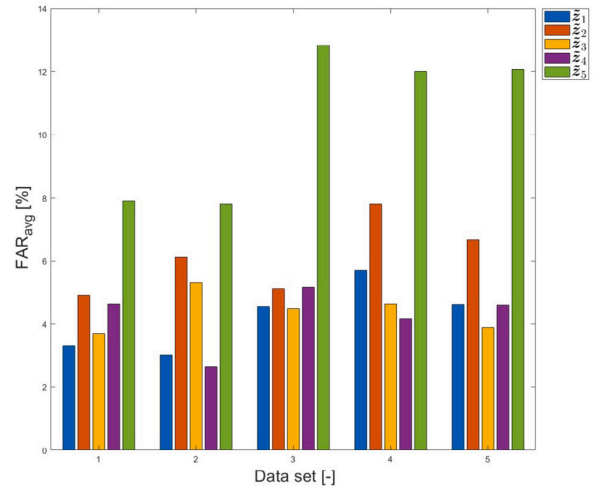

(b) FAR$_{avg}$ rates

Fig. 6. FAR (a) and FAR$_{avg}$ (b) performance of all $\tilde{\lambda}_i$ and $\tilde{\mathbf{z}}_i$ respectively on five independent NOC data sets.

6. Results discussion

The FDI robustness results are discussed first. From the results of Section 5.5, it is apparent that $\tilde{\lambda}_5$ and $\tilde{\mathbf{z}}_5$ were contaminated by process noise, given their significant deviation from the calibrated FAR. These deviations are also notably higher than the deviations displayed by the first four components. The selection of $l = 4$ for noise elimination was therefore sufficient and selecting a lower l would not have been beneficial. Consequently, the elimination of $\tilde{\lambda}_5$ and $\tilde{\mathbf{z}}_5$ from the monitoring matrix would lead to a more robust fault detection platform. Since the fault signature is constructed on this platform, the fault signature would also be more robust, thus increasing the confidence with which faults are isolated. Furthermore, the elimination of components includes computational benefits. Naturally, fewer components require less processing and smaller fault signatures reduce storage requirements for fault databases. In this case, a 20% reduction was achieved when five components are reduced to four. While this may seem minuscule when considering the size of the process in this case study, the computational benefits will become notable when applied to industrial-scale plants that contain multiple complex processes.

Table 3
Description of process faults for TAR test.

Fault number	Description
1	10% Leakage on cold water inlet of tank 1
2	20% Leakage on cold water inlet of tank 1
3	30% Leakage on cold water inlet of tank 1
4	10% Leakage on cold water inlet of tank 2
5	20% Leakage on cold water inlet of tank 2
6	30% Leakage on cold water inlet of tank 2
7	FC1 failure for tank 1
8	FC2 failure for tank 2
9	2% Temperature sensor drift of tank 1
10	5% Temperature sensor drift of tank 1
11	2% Temperature sensor drift of tank 2
12	5% Temperature sensor drift of tank 2

Regarding sensitivity, no single component is dominant for all faults. The first component has the best TAR performance for faults two and three in Fig. 6(a) and the second component dominates in fault eleven. Component four has the best TAR$_{avg}$ for fault eight, for example. Finally, component five showed the highest TAR and TAR$_{avg}$ for nine of the twelve tested faults. These nine faults differ in property, namely type, magnitude, and location. Overall, the results *suggest* that component five is the most sensitive, regardless of fault property within the scope of tested faults. However, given that other components are able to match or outperform component five in some faults, it appears that the sensitivity of each component may be a function of the unique combination of fault properties. It is concluded then that component five (and lesser components in general) are, at the least, valuable contributors to the detection of faults.

The latter conclusion on sensitivity stands in direct opposition to the argument of elimination for robustness. This is not surprising and supports the fact that a trade-off exists between sensitivity and robustness (Russel et al., 2000). It will be the duty of the practitioner to configure the EGBV FDI scheme to prioritise either better sensitivity by retaining lesser components or to have a more robust monitoring scheme by eliminating the lesser components.

7. Conclusion

In this work, it was shown that the fault detection and isolation platform of EGBV may be evaluated from a spectral theorem perspective. To this extent, the robustness and sensitivity of the EGBV components were analysed to clarify their role in the robustness and sensitivity performance of the monitoring scheme using process data from a practical pilot plant. The results show that lesser EGBV components may be ignored to the advantage of robustness and computational efficiency. However, it was also shown that the lesser components make a substantial contribution to the overall sensitivity of the scheme. Therefore, a trade-off exists between prioritising robustness and sensitivity by the elimination or inclusion of lesser EGBV components. Additionally, a formula was derived to verify the resolution of the trimmed fault signature, should the practitioner choose to remove lesser components from the monitoring structure.

It is recommended that future studies investigate the spectral theorem approach described in this paper on different and larger processes for further validation of the approach. Furthermore, a formal study should be conducted to investigate the best approach for determining the number of components l to be retained. Finally, the authors recommend the development of a theoretical basis for the uniqueness of the EGBV method's fault signatures for different faults.

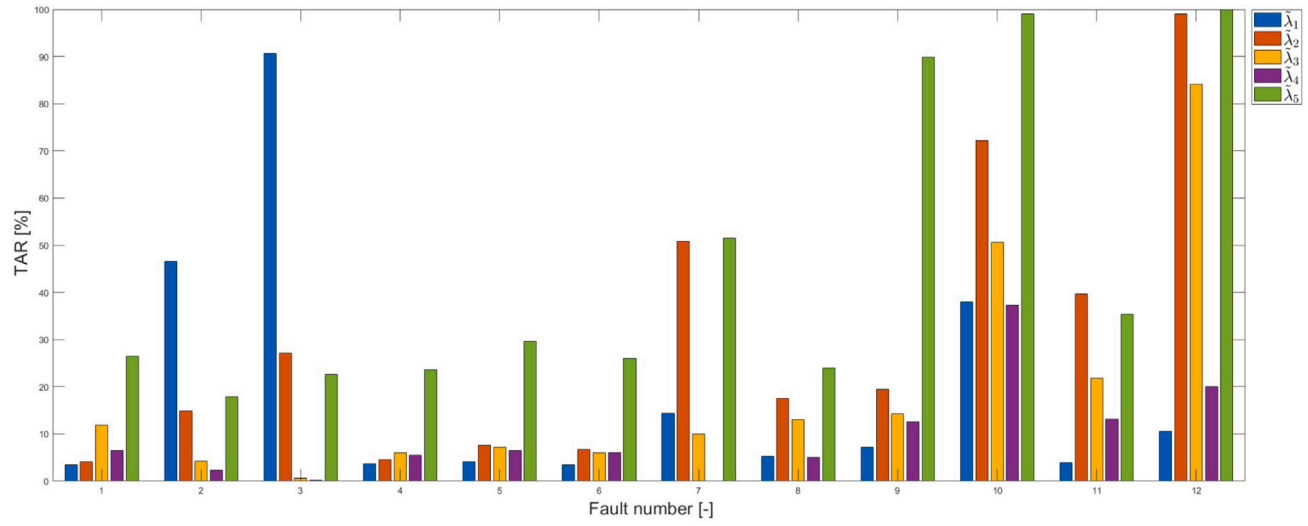

(a) TAR rates

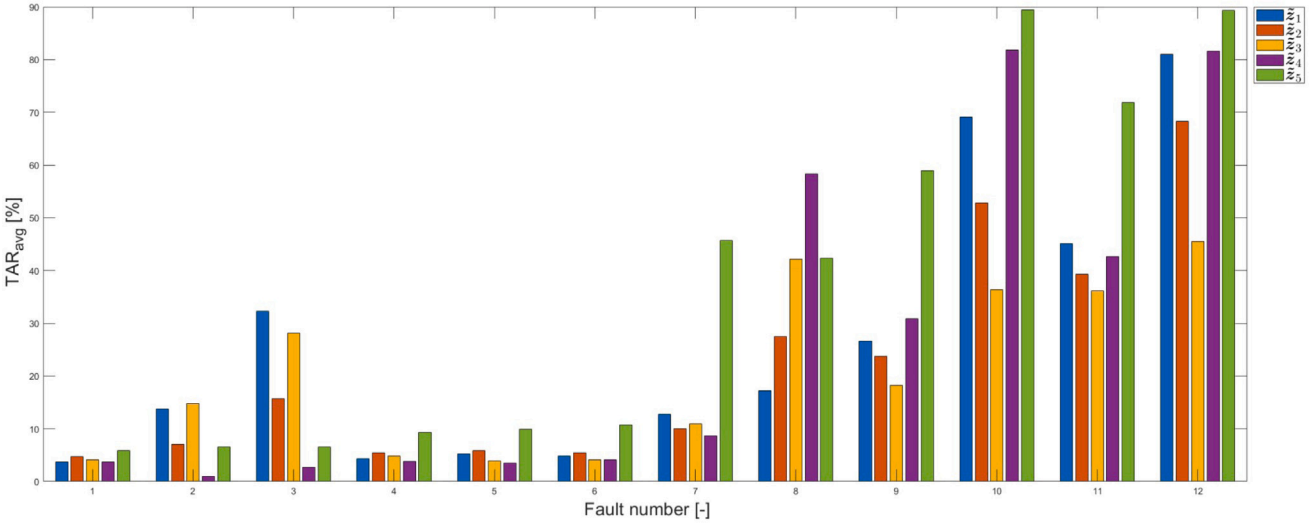

(b) TAR_{avg} rates

Fig. 7. TAR (a) and TAR_{avg} (b) performance of all $\tilde{\lambda}_i$ and $\tilde{\mathbf{z}}_i$ respectively on the twelve different process faults in Table 3.

CRediT authorship contribution statement

Wikus Wolmarans: Writing, Conceptualization. **George van Schoor:** Writing, Conceptualization. **Kenneth R. Uren:** Writing, Conceptualization.

Declaration of competing interest

The authors declare that they have no known competing financial interests or personal relationships that could have appeared to influence the work reported in this paper.

Data availability

Data will be made available on request.

Acknowledgment

This work is based on the research supported by the SASOL-NRF research grant (Grant number: 138606). Opinions expressed and conclusions arrived at are those of the authors and are not necessarily to be attributed to SASOL or the NRF.

References

Adil, M., Adbid, M., Khan, A., Mustafa, G., 2016. Comparison of PCA and FDA of coupled liquid tank system. In: 13th International Bhurban Conference on Applied Sciences & Technology. IEEE, Islamabad, pp. 225–230.

Barrett, W., 2007. Hermitian and positive definite matrices. In: Handbook of Linear Algebra. Chapman & Hall/CRC, pp. 130–134.

Çengel, Y.A., Boles, M.A., 2004. Thermodynamics: An Engineering Approach, fifth ed. McGraw-Hill, p. 28.

Chen, W., 2011. Fault Detection and Isolation in Nonlinear Systems: Observer and Energy-Balance Based Approaches (Ph.D. thesis). Universität Duisburg-Essen.

Chen, Z., Zhang, K., Shardt, Y., Ding, S., Yang, X., Yang, C., Peng, T., 2017. Comparison of two basic statistics for fault detection and process monitoring. IFAC-PapersOnLine 50 (1), 14776–14781.

Chiang, L.H., Jiang, B., Zhu, X., Huang, D., Braatz, R.D., 2015. Diagnosis of multiple and unknown faults using the causal map and multivariate statistics. J. Process Control 28, 27–39.

Dehmer, M., Emmert-Streib, F., Yongtang, S., 2017. Quantitative graph tteory: A new branch of graph theory and network science. Inform. Sci. 418–419, 575–580.

Du Rand, C.P., Van Schoor, G., 2012a. Fault diagnosis of generation IV nuclear HTGR components - part I: The error enthalpy-entropy graph approach. Ann. Nucl. Energy 40 (1), 14–24. http://dx.doi.org/10.1016/j.anucene.2011.09.013.

Du Rand, C.P., Van Schoor, G., 2012b. Fault diagnosis of generation IV nuclear HTGR components - Part II: The area error enthalpy-entropy graph approach. Ann. Nucl. Energy 41, 79–86. http://dx.doi.org/10.1016/j.anucene.2011.11.009.

Escobar, M.S., Kaneko, H., Funatsu, K., 2017. On generative topographic mapping and graph theory combined approach for unsupervised non-linear data visualization and fault identification. Comput. Chem. Eng. 98, 113–127, URL https://linkinghub.elsevier.com/retrieve/pii/S0098135416304033.

Gao, Z., Cecati, C., Ding, S.X., 2015. A survey of fault diagnosis and fault-tolerant techniques-part II: Fault diagnosis with knowledge-based and hybrid/active approaches. IEEE Trans. Ind. Electron. 62, 3768–3774.

Greyling, S., van Schoor, G., Uren, K.R., Marais, H., 2022. An energy graph eigende-composition approach to fault detection and isolation applied to a gas-to-liquids process. Comput. Chem. Eng. 168, 108040.

Hotelling, H., 1933. Analysis of a complex of statistical variables into principal components. J. Educ. Psychol. 24 (6), 417–441.

Izadi, I., Shah, S., Shook, D., Chen, T., 2009. An introduction to alarm analysis and design. IFAC Proc. Vol. 42 (8), 645–650.

Jouili, S., Tabbone, S., 2009. Attributed graph matching using local descriptions. In: Advanced Concepts for Intelligent Vision Systems. Bordeaux, pp. 1–13.

Lee, G., Song, S.O., Yoon, E.S., 2003. Multiple-fault diagnosis based on system decomposition and dynamic PLS. 42, American Chemical Society, pp. 6145–6154,

Marais, H., van Schoor, G., Uren, K., 2016. Energy-based fault detection for an autothermal reformer. IFAC-PapersOnLine 49 (7), 353–358. http://dx.doi.org/10.1016/j.ifacol.2016.07.325.

Marais, H., van Schoor, G., Uren, K.R., 2019. The merits of exergy-based fault detection in petrochemical processes. J. Process Control 74, 110–119. http://dx.doi.org/10.1016/j.jprocont.2017.11.005.

Md Nor, N., Rosmani, C., Hassan, C., Hussain, M., 2020. A review of data-driven fault detection and diagnosis methods: Applications in chemical process systems. Rev. Chem. Eng. 36 (4), 513–553.

Neser, H., van Schoor, G., Uren, K.R., 2021. Energy-based fault detection and isolation of a Brayton cycle-based HTGR power conversion unit – A comparative study. Ann. Nucl. Energy 164, 108616. http://dx.doi.org/10.1016/j.anucene.2021.108616.

Nikulshin, V., Wu, C., Nikulshina, V., 2002. Exergy efficiency calculation of energy intensive systems by graphs. Int. J. Appl. Thermodyn. 5 (2), 67–74.

Nomikos, P., MacGregor, J., 1994. Monitoring batch processes using multiway principal component analysis. AIChE J. 40 (8), 1361–1375.

Park, Y.J., Fan, S.K.S., Hsu, C.Y., 2020. A review on fault detection and process diagnostics in industrial processes. Processes 8.

Pearson, K., 1901. On lines and planes of closest fit to systems of points in space. Lond. Edinb. Dublin Philos. Mag. J. Sci. 2 (11), 559–572.

Qin, S., 2009. Data-driven fault detection and diagnosis for complex industrial processes. IFAC-PapersOnLine 42 (8), 1115–1125.

Reis, M., Gins, G., 2017. Industrial process monitoring in the big data/industry 4.0 era: From detection, to diagnosis, to prognosis. Processes 5 (3).

Russel, E., Chiang, L., Braatz, R., 2000. Data-Driven Techniques for Fault Detection and Diagnosis in Chemical Processes. p. 192.

Severson, K., Chaiwatanodom, P., Braatz, R., 2016. Perspectives on process monitoring of industrial systems. Annu. Rev. Control 42, 190–200.

Strang, G., 2009. Introduction to Linear Algebra, fourth ed. Wellesley-Cambridge Press, pp. 283–290.

Uren, K., Van Schoor, G., Auret, L., 2018. An energy-attributed graph approach for the purposes of FDI in a heated two-tank system. IFAC-PapersOnLine 1 (1).

Uren, K., Van Schoor, G., Van Eldik, M., De Bruin, J., 2020. An energy graph-based approach to fault diagnosis of a transcritical CO2 heat pump. Energies 13 (1789), 1–34.

van Graan, S., van Schoor, G., Uren, K.R., 2017. Graph matching as a means to energy-visualisation of a counter-flow heat exchanger for the purpose of fault diagnosis. IFAC-PapersOnLine 50 (1), 2842–2847. http://dx.doi.org/10.1016/j.ifacol.2017.08.637.

van Schoor, G., Uren, K., 2018. A vision of energy-based visualisation of large scale industrial systems for the purposes of condition monitoring. In: 31st Conference on Condition Monitoring and Diagnostic Engineering Management. pp. 1–10.

Van Schoor, G., Uren, K., Van Wyk, M., Van Vuuren, P., Du Rand, C., 2014. An energy perspective on modelling, supervision, and control of large-scale industrial systems: Survey and framework. IFAC Proc. Vol. (IFAC-PapersOnline) 19, 6692–6703.

Venkatasubramanian, V., Rengaswamy, R., Kavuri, S., 2003a. A review of process fault detection and diagnosis Part II : Qualitative models and search strategies. Comput. Chem. Eng. 27, 313–326.

Venkatasubramanian, V., Rengaswamy, R., Kavuri, S., Yin, K., 2003b. A review of process fault detection and diagnosis Part III: Process history based methods. Comput. Chem. Eng. 27, 327–346.

Venkatasubramanian, V., Rengaswamy, R., Yin, K., Kavuri, S., 2003c. A review of process fault detection and diagnosis part I: Quantitative model-based methods. Comput. Chem. Eng. 27 (3), 293–311.

Wilson, R.J., 1996. Introduction to Graph Theory, fourth ed. Longman Group Ltd, Essex, pp. 1–146.

Wilson, D.R., Martinez, T., 1997. Improved heterogeneous distance functions. J. Artificial Intelligence Res. 6, 1–34.

Yin, S., Ding, S., Haghani, A., Hao, H., Zhang, P., 2012. A comparison study of basic data-driven fault diagnosis and process monitoring methods on the benchmark Tennessee Eastman process. J. Process Control 22 (9), 1567–1581.